

Design sensitivity analysis and optimization for minimizing springback of sheet-formed part

Kiyoung Yi^{1,‡}, K. K. Choi^{1,*}, Nam H. Kim^{2,¶} and Mark E. Botkin^{3,||}

¹*Department of Mechanical and Industrial Engineering, The University of Iowa, Iowa City, IA 52242, U.S.A.*

²*Department of Mechanical and Aerospace Engineering, University of Florida, Gainesville, FL 32611, U.S.A.*

³*Vehicle Development Research Lab, GM R&D and Strategic Planning, Warren, MI 48090, U.S.A.*

SUMMARY

The springback is a manufacturing defect in the stamping process and causes difficulty in product assembly. An impediment to the use of lighter-weight, higher-strength materials in manufacturing is relative lack of understanding about how these materials respond to complex forming processes. The springback can be reduced by using an optimized combination of die, punch, and blank holder shapes together with friction and blank-holding force. An optimized process can be determined using a gradient-based optimization to minimize the springback. For an effective optimization of the stamping process, development of an efficient design sensitivity analysis (DSA) for the springback with respect to these process parameters is crucial. A continuum-based shape and configuration DSA method for the stamping process has been developed using a non-linear shell model. The material derivative is used to develop the continuum-based design sensitivity. The design sensitivity equation is solved without iteration at each converged load step in the finite deformation elastoplastic non-linear analysis with frictional contact, which makes sensitivity calculation very efficient. Numerical implementation of the proposed shape and configuration DSA method is performed using the meshfree method. The accuracy and efficiency of the proposed method are illustrated by minimizing the springback in a benchmark S-rail problem. Copyright © 2007 John Wiley & Sons, Ltd.

Received 8 December 2006; Accepted 18 December 2006

KEY WORDS: stamping process; springback; non-linear shell; meshfree method; finite deformation elastoplasticity; frictional contact; design sensitivity analysis; design optimization

*Correspondence to: K. K. Choi, Department of Mechanical and Industrial Engineering, The University of Iowa, Iowa City, IA 52242, U.S.A.

†E-mail: kkchoi@ccad.uiowa.edu

‡Graduate Research Assistant.

§Roy J. Carver Professor.

¶Assistant Professor.

||Principal Research Engineer.

Contract/grant sponsor: General Motors Corporation

1. INTRODUCTION

The stamping process was a major industrial breakthrough that made mass production of various products, which range from automobiles to home appliances, possible. However, the springback in metal stamping is still very much problematic such that it requires a trial-and-error process to remove it, which is very expensive. For example, a large size die for a passenger vehicle side door could cost up to one million dollars. These days, carmakers face ever more frequently the phenomenon of the springback, especially with new high-strength steels. As a result, industries need a better understanding of how to compensate for the springback in the stamping process especially for lightweight materials such as aluminium and high-strength steel.

The stamping process involves a combination of elastoplastic bending and stretching deformation of the blank sheet through frictional contact. These deformations can lead to large amounts of the springback after the punch, die, blank holder are removed. The springback behaviour is very complex and is affected by many factors including material properties, clearance between punch and die, thickness of the blank sheet, the tool (die, punch, and blank holder) shape, and blank-holding force. Simulation of such behaviours using numerical methods such as finite element analysis (FEA) is still very much challenging problem, let alone design sensitivity analysis (DSA). Thus, extensive research efforts on the simulation of stamping process have been performed. The earliest studies on FEA of sheet forming are made by Gotoh and Ishie [1], Wang and Budiansky [2], and Wifi [3]. The first two works utilized an elastoplastic law, while the latter used a rigid-plastic law. Wang and Budiansky [2] used membrane element and Wifi [3] used continuum element. The FEA was extended to three-dimensional applications by Tang *et al.* [4] and Toh and Kobayashi [5, 6]. All studies mentioned above are of static implicit or static explicit type. The dynamic explicit methods have their roots in the study of Belytschko and Mullen [7]. Application to deformation mechanics is given in the work of Benson and Hallquist [8]. Batoz *et al.* [9] proposed the inverse approach (IA). Recent benchmark tests and accompanying papers [10–13] illustrate the state of the art in simulation of stamping process using FEA.

There have been several attempts to reduce the springback problem. For example, Wenner [14] showed that tensile stretching stresses superimposed on the bending stresses of an elastoplastic material could reduce the springback in two-dimensional formed parts. Liu [15] has proposed variations of the blank-holding force during the forming process to provide tensile pre-loading or post-loading on the formed part for springback reduction. However, it is not always possible to transmit high tensile forces to all parts of a blank sheet with complicated geometry without causing failure by tearing of the formed part. Karafillis and Boyce [16] proposed a methodology for tool shape design based on the inverse springback calculation. In their method, the traction distribution on the formed part is calculated at the fully loaded stage and this traction distribution was used to elastically load a part to give the desired die shape. However, these methods cannot be easily applied to the stamping process of complex formed part shape [17, 18]. Gan and Wagoner [17] and Gan *et al.* [18] used the displacement vectors at each node to minimize the springback by adjusting the trial die design until the target part shape is achieved.

In recent years, DSA has been used for the stamping process design. For example, Yang *et al.* [19] optimized hydroforming process by applying a gradient-based method including sensitivity analysis. Naceur *et al.* [20] optimized drawbead restraining force to improve the sheet metal formability in deep drawing process. Sosnowski *et al.* [21] presented direct differentiation method of DSA to optimize two simple contact bodies. As it is pointed out by Choi *et al.* [22], there are three approaches for DSA: the finite difference method (FDM), discrete method, and

continuum-based method. Among them, the continuum-based method differentiates the variational equation before discretization and thus is more efficient and accurate than the two other methods, although it requires lengthy and sophisticated mathematical derivations. In this paper, a continuum-based DSA method for a stamping process has been developed. The DSA for the stamping process is quite challenging because it requires sensitivity analysis of a shell structure with three non-linearities: elastoplasticity, finite deformation, and frictional contact. Detailed discussion of DSA for a finite deformation elastoplastic shell structure is developed by Yi *et al.* [23], where the continuum-based DSA method is developed using the elastoplastic return-mapping algorithm [24] along with the Hughes–Winget’s incrementally objective integration algorithm [25–27].

By integrating the DSA results by Yi *et al.* [23] and the newly developed DSA method for the frictional contact problem in this paper, a continuum-based DSA method for a finite deformation elastoplastic non-linear shell structure with frictional contact is developed for application to the stamping process design. Several contact algorithms are available: the Lagrange multiplier, penalty function, and the direct node projection [28, 29]. Among these algorithms for frictional contact enforcement, the penalty function is used in this paper. Therefore, for DSA, a penalty-regularized variational equation [30] is differentiated with respect to the stamping process parameters. The material derivative that is consistent with the frictional return-mapping scheme is derived. A piecewise-linear contact surface causes a significant amount of difficulty in the Newton-type iterative method because it lacks continuity across the surface boundary. Thus, computer-aided design (CAD) geometry-based representations of die and punch surfaces are used in this paper to alleviate the difficulty by providing smooth contact surface.

For DSA of the stamping process, the sensitivity equation uses the same tangent stiffness matrix as the response analysis, which is already decomposed during non-linear analysis, and only a substitution process using fictitious load vectors is required. Therefore, the computational cost of DSA is much less than that of the response analysis, which makes the design optimization process very efficient. Numerical implementation of the proposed shape and configuration DSA method is carried out using the meshfree method. Accuracy and efficiency of the proposed method are demonstrated by minimizing the springback of the benchmark S-rail forming problem.

2. GEOMETRIC REPRESENTATIONS OF TOOLS AND BLANK SHEET

In the stamping process, deformations of the tools (rigid punch, die, and blank holder) are generally ignorable. Therefore, in the numerical analysis, these tools can be modelled as rigid bodies and their discretization is not needed. Only the blank sheet is modelled as the shell structure and discretized. A CAD geometry-based representation is utilized for both the tool surface and the shear deformable shell structure. Since the CAD surface representation used in this paper has C^1 -continuity, its use for the tool surface provides a continuous contact force and surface normal vector, as well as a valid contact tangent stiffness matrix. The CAD geometry-based representation of the tool surface alleviates significant amount of difficulty of the piecewise-linear contact surface model often used in FEA. In addition, since no element information is generated in the meshfree method (which is used in this paper for numerical analysis), the surface information from the CAD geometry is necessary for constructing the surface normal vector and the mapping from global to local co-ordinates.

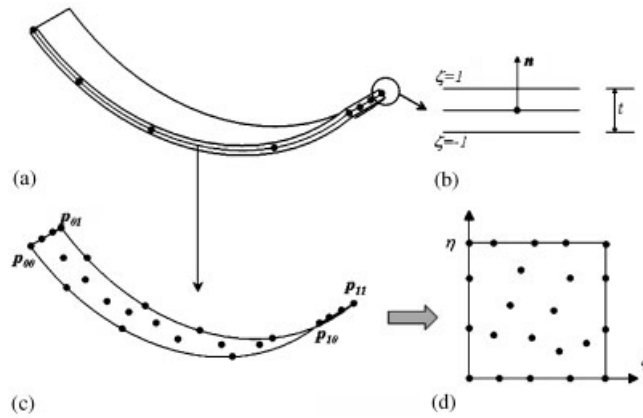


Figure 1. Shell structure.

2.1. Tool surface representation

A CAD geometry-based representation is utilized for the tool surface. Figure 1(c) and (d) show the general surface geometry in a three-dimensional space and its transformation into parametric co-ordinate. In the CAD software, a general surface geometry in a three-dimensional space can be represented by using two parameters as [31, 32]

$$\mathbf{x}^n(\xi, \eta) = \mathbf{U}(\xi)^T \mathbf{M} \mathbf{G} \mathbf{M}^T \mathbf{W}(\eta) \tag{1}$$

where $\mathbf{U}(\xi) = [\xi^3, \xi^2, \xi, 1]^T$ and $\mathbf{W}(\eta) = [\eta^3, \eta^2, \eta, 1]^T$ are vectors in the parametric co-ordinates, \mathbf{M} is the matrix defined as

$$\mathbf{M} = \begin{bmatrix} 2 & -2 & 1 & 1 \\ -3 & 3 & -2 & -1 \\ 0 & 0 & 1 & 0 \\ 1 & 0 & 0 & 0 \end{bmatrix} \tag{2}$$

and \mathbf{G} is the surface geometric matrix defined as

$$\mathbf{G} = \begin{bmatrix} \mathbf{P}_{00} & \mathbf{P}_{01} & \mathbf{P}_{00}^\eta & \mathbf{P}_{01}^\eta \\ \mathbf{P}_{10} & \mathbf{P}_{11} & \mathbf{P}_{10}^\eta & \mathbf{P}_{11}^\eta \\ \mathbf{P}_{00}^\xi & \mathbf{P}_{01}^\xi & \mathbf{P}_{00}^{\xi\eta} & \mathbf{P}_{01}^{\xi\eta} \\ \mathbf{P}_{10}^\xi & \mathbf{P}_{11}^\xi & \mathbf{P}_{10}^{\xi\eta} & \mathbf{P}_{11}^{\xi\eta} \end{bmatrix} \tag{3}$$

where \mathbf{p}_{ij} are co-ordinates of the corner points on the surface, \mathbf{p}_{ij}^ξ and \mathbf{p}_{ij}^η are the tangent vectors in ξ and η directions, and $\mathbf{p}_{ij}^{\xi\eta}$ are the twist vectors.

2.2. Kinematics of the blank sheet

A general shell structure is represented by the neutral surface geometry and thickness data at each point as shown in Figures 1(a)–(c). The neutral surface geometry can also be represented using Equation (1). The surface representation method in Equation (1) provides good flexibility from the computational viewpoint. For example, the normal vector on the surface at (ξ, η) can be obtained as

$$\mathbf{n}(\xi, \eta) = \frac{\mathbf{x}_{,\xi}^n \times \mathbf{x}_{,\eta}^n}{\|\mathbf{x}_{,\xi}^n \times \mathbf{x}_{,\eta}^n\|} \quad (4)$$

where, from Equation (1),

$$\mathbf{x}_{,\xi}^n = \mathbf{U}_{,\xi}^T(\xi) \mathbf{MGM}^T \mathbf{W}(\eta) \quad (5)$$

$$\mathbf{x}_{,\eta}^n = \mathbf{U}(\xi)^T \mathbf{MGM}^T \mathbf{W}_{,\eta}(\eta) \quad (6)$$

For the shell structure with thickness $t(\xi, \eta)$, any points within the structure can be expressed by

$$\mathbf{x}(\xi, \eta, \zeta) = \mathbf{U}(\xi)^T \mathbf{MGM}^T \mathbf{W}(\eta) + \zeta \frac{t}{2} \mathbf{n}(\xi, \eta) \quad (7)$$

where $\zeta = [-1, 1]$ is the third parametric co-ordinate in the thickness direction, and $\mathbf{n}(\xi, \eta)$ is the outward unit vector of the surface, obtained from Equation (4). The Jacobian of the mapping relation between physical and parametric co-ordinate can be obtained, from the relation in Equation (7), as

$$\begin{aligned} \mathbf{x}_{,\xi} &= \mathbf{U}_{,\xi}^T \mathbf{MGM}^T \mathbf{W} + \zeta \frac{t}{2} \mathbf{n}_{,\xi} \\ \mathbf{x}_{,\eta} &= \mathbf{U}^T \mathbf{MGM}^T \mathbf{W}_{,\eta} + \zeta \frac{t}{2} \mathbf{n}_{,\eta} \\ \mathbf{x}_{,\zeta} &= \frac{t}{2} \mathbf{n} \end{aligned} \quad (8)$$

The notations $\mathbf{x} = [x, y, z]^T = [x_1, x_2, x_3]^T$ and $\boldsymbol{\chi} = [\xi, \eta, \zeta]^T = [\xi_1, \xi_2, \xi_3]^T$ are used in the following derivations. Using these notations, the Jacobian of the mapping can be represented by

$$\mathbf{J} = \frac{\partial x_i}{\partial \xi_j} \quad (9)$$

For the shell structure, the constitutive relation is given in body-fixed, local co-ordinate, whereas a displacement–strain relation is provided in global co-ordinate. The unit vectors in the local co-ordinate are calculated as

$$\mathbf{l} = \frac{\mathbf{x}_{,\xi}^n}{\|\mathbf{x}_{,\xi}^n\|}, \quad \mathbf{n} = \frac{\mathbf{x}_{,\xi}^n \times \mathbf{x}_{,\eta}^n}{\|\mathbf{x}_{,\xi}^n \times \mathbf{x}_{,\eta}^n\|}, \quad \mathbf{m} = \mathbf{n} \times \mathbf{l} \quad (10)$$

Using the relation in Equation (10), the co-ordinate transformation can be obtained as

$$\mathbf{x} = \begin{bmatrix} l_1 & m_1 & n_1 \\ l_2 & m_2 & n_2 \\ l_3 & m_3 & n_3 \end{bmatrix} \mathbf{x}' \tag{11}$$

where \mathbf{x}' is the global co-ordinate of the corresponding point \mathbf{x} in the local co-ordinate.

3. CONTACT ANALYSIS

A detailed discussion of the variational equation for the non-linear elastoplastic shell with finite deformation and continuum-based DSA method is presented by Yi *et al.* [23], where the structural energy form, load linear form, and linearized structural energy form are derived. These results are shown in Figure 2, which will be used in this paper to derive the variation equation for the stamping process, by integrating with the contact variational form derived in this section.

In this section, contact analysis between a shell structure (a blank sheet) and tools (rigid punch, die, and blank holder) is described in continuum formulation. Figure 3 illustrates the contact kinematics between two surfaces, represented by Γ_x^1 and Γ_x^2 , where Γ_x^1 is designated as a slave surface, while Γ_x^2 is designated as a master surface. In the stamping problem, the blank sheet is referred to as the slave body and the punch, die, and blank holder are referred to as the master

Structural Energy Form :	$a_{\Omega}({}^{n+1}\mathbf{z}, \bar{\mathbf{z}}) = \int_{{}^{n+1}\Omega} \bar{z}_{i, n+1, x_j} {}^{n+1}\sigma_{ij} d\Omega$
Load Linear Form :	$\ell_{\Omega}(\bar{\mathbf{z}}) = \int_{{}^{n+1}\Omega} \bar{z}_i f_i^B d\Omega$
Linearized Structural Energy Form :	
	$a_{\Omega}^*({}^{n+1}\mathbf{z}; \Delta\mathbf{z}, \bar{\mathbf{z}}) = \int_{{}^{n+1}\Omega} \bar{z}_{i, n+1, x_j} [C_{ijkl}^{alg} + \delta_{kl}\sigma_{ij} - \delta_{ij}\sigma_{kl}] \Delta z_{k, n+1, x_l} d\Omega$

Figure 2. Structural energy and load linear forms.

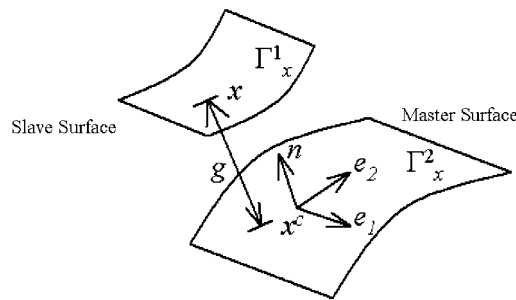


Figure 3. Contact kinematics.

bodies. The contact constraints are imposed such that the points on Γ_x^1 cannot penetrate into Γ_x^2 . The master surface is represented by the two parameters of the CAD geometric surface as $\mathbf{x}(\xi_1, \xi_2)$. Therefore, two tangential vectors and a normal vector on the master surface are defined as

$$\mathbf{e}_1 = \mathbf{x}_{,1}, \quad \mathbf{e}_2 = \mathbf{x}_{,2}, \quad \mathbf{n} = \mathbf{e}_1 \times \mathbf{e}_2 / \|\mathbf{e}_1 \times \mathbf{e}_2\| \tag{12}$$

where $\mathbf{x}_{,\alpha} = \partial \mathbf{x} / \partial \xi_\alpha$, $\alpha = 1, 2$. Note that \mathbf{e}_1 and \mathbf{e}_2 are not necessarily orthogonal to each other, but are tangent to the master surface.

One of the most important steps in the contact analysis is to locate the contact point in accurate and efficient way. The contact point $\mathbf{x}^c \in \Gamma_x^2$ corresponding to the slave point $\mathbf{x} \in \Gamma_x^1$ is determined first using an optimization for minimum distance, and then refined using the consistency condition

$$\mathbf{e}_\alpha \cdot (\mathbf{x} - \mathbf{x}^c) = 0, \quad \alpha = 1, 2 \tag{13}$$

Note that \mathbf{x}^c is the closest projection point corresponding to \mathbf{x} . Using the normal gap function, which is the normal distance between two bodies, the impenetrability condition can be imposed as

$$g = \mathbf{n} \cdot (\mathbf{x} - \mathbf{x}^c) \geq 0 \tag{14}$$

It is well known that the contact variational inequality is equivalent to the constrained minimization problem, which can be approximated using the Lagrange multiplier or penalty method. In this paper, the penalty method is used without introducing additional unknowns in the variational governing equation.

If a region denoted $\Gamma^c (\subset \Gamma_x^1)$ exists that violates the impenetrability condition of Equation (14), then this region is penalized using a penalty function, which is defined as

$$P = \frac{1}{2} \omega_n \int_{\Gamma^c} g^2 \, d\Gamma \tag{15}$$

where ω_n is the penalty parameter. Let the symbol ‘over-bar’ denote a variation of the quantity such that $\bar{\mathbf{z}}$ represents a variation of the displacement \mathbf{z} . The variation of the penalty function in Equation (15) contains the variation of the gap function, which can be obtained from its definition as

$$\bar{g} = \mathbf{n} \cdot (\bar{\mathbf{z}} - \bar{\mathbf{z}}^c) \equiv \mathbf{n} \cdot \hat{\mathbf{z}} \tag{16}$$

where the notations $\hat{\mathbf{z}} = \mathbf{z} - \mathbf{z}^c$ and $\hat{\mathbf{z}} = \bar{\mathbf{z}} - \bar{\mathbf{z}}^c$ are used for the relative displacement and its variation between two contact points. Note that the variation of the normal vector \mathbf{n} vanishes because it is orthogonal to the vector $(\mathbf{z} - \mathbf{z}^c)$.

The variation of the penalty function becomes the contact variational form, which is defined as

$$b_N^{(n+1)}(\mathbf{z}, \bar{\mathbf{z}}) \equiv \bar{P} = \omega_n \int_{\Gamma^c} g \bar{g} \, d\Gamma \tag{17}$$

where $\omega_n g$ corresponds to the compressive normal force. The left superscript ‘ $n + 1$ ’ denotes the configuration at time t_{n+1} .

By combining Equation (17) with the structural energy form $a_\Omega^{(n+1)}(\mathbf{z}, \bar{\mathbf{z}})$ and load linear form $\ell_\Omega(\bar{\mathbf{z}})$ shown in Figure 2, the finite deformation elastoplastic non-linear variational governing equation for the penalized contact condition becomes

$$a_\Omega^{(n+1)}(\mathbf{z}, \bar{\mathbf{z}}) + b_N^{(n+1)}(\mathbf{z}, \bar{\mathbf{z}}) = \ell_\Omega(\bar{\mathbf{z}}) \quad \forall \bar{\mathbf{z}} \in Z \tag{18}$$

where

$$Z = \{\mathbf{z} \in [H^1(\Omega)]^3 \mid \mathbf{z}(\mathbf{x}) = 0, \mathbf{x} \in \Gamma_g\} \quad (19)$$

is the space of kinematically admissible displacement, and $H^1(\Omega)$ is the first-order Sobolev space and Γ_g is the essential boundary where the displacement is prescribed. Note that even if the structure encounters only elastic deformation, Equation (18) is non-linear since the inequality constraint is imposed throughout the penalty method.

In this paper, the return-mapping algorithm on the subspace defined by the zero-normal stress condition is used for elastoplastic integration. In order to handle the finite deformation, the Hughes–Winget’s incrementally objective integration scheme is used [23]. The non-linear equation (18) is first linearized, and then solved using a Newton iterative method to obtain the solution. The linearized structural energy form, $a_{\Omega}^{*(n+1)}(\mathbf{z}; \Delta\mathbf{z}, \bar{\mathbf{z}})$, is given in Figure 2.

The linearization of contact variational form, $b_N^{*(n+1)}(\mathbf{z}; \Delta\mathbf{z}, \bar{\mathbf{z}})$, will be derived in next section in the process of DSA. By combining the linearization of the contact variational form with that of the structural energy form, the incremental equation becomes

$$\begin{aligned} & a_{\Omega}^{*(n+1)}(\mathbf{z}^k; \Delta\mathbf{z}^{k+1}, \bar{\mathbf{z}}) + b_N^{*(n+1)}(\mathbf{z}^k; \Delta\mathbf{z}^{k+1}, \bar{\mathbf{z}}) \\ & = \ell_{\Omega}(\bar{\mathbf{z}}) - a_{\Omega}^{(n+1)}(\mathbf{z}^k, \bar{\mathbf{z}}) - b_N^{(n+1)}(\mathbf{z}^k, \bar{\mathbf{z}}) \quad \forall \bar{\mathbf{z}} \in Z \end{aligned} \quad (20)$$

where the right superscript k denotes the current iteration counter. For a given load step, Equation (20) is solved iteratively until the residual force vanishes. After convergence, the decomposed tangent stiffness matrix is stored to be used for DSA. The continuum-based DSA method for a finite deformation elastoplastic shell structure is developed by Yi *et al.* [23], which will be used here to combine with DSA of the frictional contact problem.

4. DESIGN SENSITIVITY ANALYSIS OF SHELL CONTACT PROBLEM

For design of the stamping process, the design variables are the shape of the stamped workpiece (for multistage stamping process) and tool surfaces (punch, die, and blank holder). Even when the shape of the workpiece is initially flat and thus does not render a shape design, the DSA formulation must include the design velocity field of the workpiece because the updated Lagrangian formulation is used for the non-linear analysis. For DSA of the contact problem, instead of differentiating the contact variational inequality, the penalty-approximated variational equation is differentiated with respect to the design variable.

4.1. Material derivative formulas

In shape and configuration DSA, a material point ${}^0\mathbf{x}$ is moved to a new point ${}^0\mathbf{x}_{\tau} (= {}^0\mathbf{x} + \tau {}^0\mathbf{V})$ due to design perturbation. A design velocity field ${}^0\mathbf{V}$ of the undeformed configuration represents the direction of the design perturbation, and τ is a scalar parameter that determines the perturbation size. In the updated Lagrangian formulation, the reference frame is updated after each incremental analysis using the following relation:

$${}^n\mathbf{x} = {}^0\mathbf{x} + {}^n\mathbf{z} \quad (21)$$

where ${}^n\mathbf{x}$ is spatial co-ordinate at time t_n and ${}^n\mathbf{z}$ is the sum of the incremental displacement up to time t_n . By differentiating the above relation, the following design velocity update formula is obtained:

$$\frac{d}{d\tau}({}^n\mathbf{x}_\tau) \Big|_{\tau=0} = \frac{d}{d\tau}({}^0\mathbf{x}_\tau + {}^n\mathbf{z}_\tau) \Big|_{\tau=0} = {}^0\mathbf{V} + {}^n\dot{\mathbf{z}} = {}^n\mathbf{V} \tag{22}$$

The superposed dot will be used to denote the material derivative of the variable. Note that even when the shape of the slave surface (workpiece) is not a design variable, and thus initial design velocity field, ${}^0\mathbf{V}$, is zero, the design velocity field at time t_n is non-zero due to ${}^n\dot{\mathbf{z}}$.

Using the relation in Equation (22), the material derivative of the structural point on the slave surface at the current configuration becomes

$$\frac{d}{d\tau}({}^{n+1}\mathbf{x}_\tau) \Big|_{\tau=0} = \frac{d}{d\tau}({}^n\mathbf{x}_\tau + \Delta\mathbf{z}_\tau) \Big|_{\tau=0} = {}^n\mathbf{V} + \Delta\dot{\mathbf{z}} \tag{23}$$

On the other hand, the perturbation of the contact point on the master surface (tool surface) can be obtained by using the chain rule and by perturbing the natural co-ordinate corresponding to the contact point in the tangential direction as

$$\frac{d}{d\tau}({}^{n+1}\mathbf{x}_\tau^c) \Big|_{\tau=0} = {}^n\mathbf{V}^c + \Delta\dot{\mathbf{z}}^c + \mathbf{e}_\alpha \dot{\zeta}_\alpha \tag{24}$$

where a summation rule is used for the repeated indices.

The material derivatives of the structural energy form are [23]

$$\frac{d}{d\tau}[a_\Omega({}^{n+1}\mathbf{z}_\tau, \bar{\mathbf{z}}_\tau)] \Big|_{\tau=0} = a_\Omega^*({}^{n+1}\mathbf{z}; \Delta\dot{\mathbf{z}}, \bar{\mathbf{z}}) + a'_V({}^{n+1}\mathbf{z}, \bar{\mathbf{z}}) \tag{25}$$

where $a_\Omega^*({}^{n+1}\mathbf{z}; \Delta\dot{\mathbf{z}}, \bar{\mathbf{z}})$ is the same form as the linearized energy form in Equation (20) by substituting $\Delta\mathbf{z}^k$ for $\Delta\dot{\mathbf{z}}$. $a'_V({}^{n+1}\mathbf{z}, \bar{\mathbf{z}})$ is the structural fictitious load form as given in Figure 4, which includes all known terms from the response analysis and DSA up to the previous time step and its expression. The material derivative of the load linear form is obtained by Yi *et al.* [23] as

$$\frac{d}{d\tau}[\ell_\Omega(\bar{\mathbf{z}}_\tau)] \Big|_{\tau=0} = \int \int \int_{n+1}\Omega \bar{z}_i f_i^B \text{div } V \, d\Omega \equiv \ell'_V(\bar{\mathbf{z}}) \tag{26}$$

Structural Fictitious Load Form :

$$a'_V({}^{n+1}\mathbf{z}, \bar{\mathbf{z}}) = \int_\Omega \left[\mathcal{E}'_{ij}(\bar{\mathbf{z}}) \sigma_{ij} + \bar{z}_{i,n+1,x_j} C_{ijkl}^{\text{alg}} \right. \\ \left. + \bar{z}_{i,n+1,x_j} \sigma_{ij}^{\text{fic}} + \bar{z}_{i,n+1,x_j} \sigma_{ij} \text{div}^n V \right] d\Omega$$

where C_{ijkl}^{alg} and $\sigma_{ij}^{\text{fic-s}}$ are given in equations (89) and (90), respectively in Yi *et al.* [23]

Figure 4. Fictitious load form for DSA.

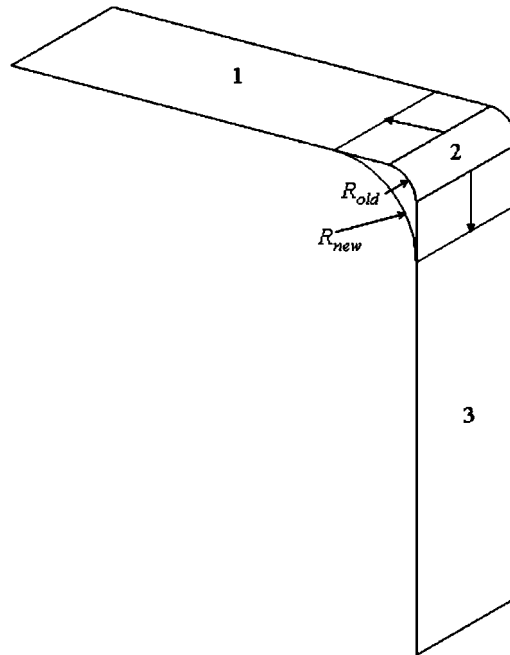


Figure 5. Example of die composed of three surfaces.

4.2. Design velocity field computation

The computation of design velocity fields ${}^0\mathbf{V}$ and ${}^0\mathbf{V}^c$ are directly related to the parametric representation of the surface, as given in (1). For example, Figure 5 shows die geometry, which is composed of three surfaces. Each surface is characterized by its surface geometric matrix $\mathbf{G}_{i=1,2,3}$ as in (3). If the corner radius R is considered as a design parameter, the design dependence of the surface is written as

$${}^0\mathbf{x}_i^c(R) = \mathbf{U}(\xi)^T \mathbf{M} \mathbf{G}_i(R) \mathbf{M}^T \mathbf{W}(\eta), \quad i = 1, 2, 3 \quad (27)$$

Since geometric matrix $\mathbf{G}_i(R)$ is a function of the corner radius R , the design velocity can be obtained by perturbing R to $R + \tau \delta R$, and then differentiating with respect to τ as

$$\begin{aligned} {}^0\mathbf{V}_i^c &= \left. \frac{d{}^0\mathbf{x}_i^c(R + \tau \delta R)}{d\tau} \right|_{\tau=0} = \mathbf{U}(\xi)^T \mathbf{M} \left(\frac{\partial \mathbf{G}_i}{\partial R} \delta R \right) \mathbf{M}^T \mathbf{W}(\eta) \\ &= \mathbf{U}(\xi)^T \mathbf{M} (\mathbf{G}_i^{\text{new}} - \mathbf{G}_i) \mathbf{M}^T \mathbf{W}(\eta) \end{aligned} \quad (28)$$

where $\mathbf{G}_i^{\text{new}}$ is a geometric matrix of each surface when the corner radius is changed to R_{new} using the CAD geometry.

Suppose the contact surface Γ^c change its shape due to the die shape design perturbation. The contact form in Equation (17) depends on the design in two ways: explicitly through the contact

surface design change and implicitly through the response \mathbf{z} . The material derivative of the contact form can be obtained as

$$\frac{d}{d\tau}[b_N(^{n+1}\mathbf{z}, \bar{\mathbf{z}})]\Big|_{\tau=0} = \omega_n \int_{\Gamma_c} [\dot{g}\bar{g} + g\dot{\bar{g}} + gg\kappa^n V_n] d\Gamma \quad (29)$$

where κ is the curvature of the master surface, and ${}^n\mathbf{V}$ is the normal component of the design velocity. For DSA, \dot{g} and $\dot{\bar{g}}$ need to be expressed in terms of the implicit term $\Delta\dot{\mathbf{z}}$ and the explicit term ${}^n\mathbf{V}$. From its definition in Equation (14), the material derivative of the gap function can be obtained as

$$\dot{g} = \mathbf{n} \cdot (\Delta\dot{\mathbf{z}} + {}^n\hat{\mathbf{V}}) \quad (30)$$

where $\Delta\dot{\mathbf{z}} \equiv \Delta\dot{\mathbf{z}} - \Delta\dot{\mathbf{z}}^c$ and ${}^n\hat{\mathbf{V}} \equiv {}^n\mathbf{V} - {}^n\mathbf{V}^c$. However, the derivation of $\dot{\bar{g}}$ is not straightforward and the relation of $\bar{\mathbf{z}} = \bar{g}\mathbf{n} + g\bar{\mathbf{n}} + \mathbf{e}_\alpha \bar{\xi}_\alpha$ is needed to make the stiffness matrix symmetric. By taking the material derivative of \bar{g} in Equation (16),

$$\dot{\bar{g}} = -\mathbf{n} \cdot \bar{\mathbf{z}}_{,\alpha} \dot{\xi}_\alpha - (\mathbf{n} \cdot \dot{\mathbf{e}}_\alpha) \bar{\xi}_\alpha + g(\mathbf{n} \cdot \dot{\mathbf{e}}_\alpha) m_{\alpha\beta}^{-1} (\mathbf{n} \cdot \bar{\mathbf{e}}_\beta) \quad (31)$$

where $m_{\alpha\beta} = \mathbf{e}_\alpha \cdot \mathbf{e}_\beta$. In Equation (31),

$$\dot{\mathbf{e}}_\alpha \equiv \frac{d}{d\tau} (^{n+1}\mathbf{x}_{,\alpha}^c) \Big|_{\tau=0} = \Delta\dot{\mathbf{z}}_{,\alpha}^c + {}^n\mathbf{V}_{,\alpha}^c + {}^{n+1}\mathbf{x}_{,\alpha\beta}^c \dot{\xi}_\beta \quad (32)$$

The expression of $\dot{\xi}_\beta$ can be obtained from the consistency condition in Equation (13) as

$$\begin{aligned} \dot{\xi}_\beta &= A_{\alpha\beta}^{-1} (\Delta\dot{\mathbf{z}} \cdot \mathbf{e}_\alpha) + A_{\alpha\beta}^{-1} ({}^n\hat{\mathbf{V}} \cdot \mathbf{e}_\alpha + g\mathbf{n} \cdot {}^n\mathbf{V}_{,\alpha}^c) \\ &\equiv \xi_\beta(\Delta\dot{\mathbf{z}}) + \xi_\beta({}^n\mathbf{V}) \end{aligned} \quad (33)$$

where $A_{\alpha\beta} = m_{\alpha\beta} - g\mathbf{n} \cdot {}^{n+1}\mathbf{x}_{,\alpha\beta}^c$. By using the relations from Equations (30) to (33), the material derivative of the contact variational form can be separated into two parts: the implicitly dependent and the explicitly dependent parts as

$$\frac{d}{d\tau}[b_N(^{n+1}\mathbf{z}_\tau, \bar{\mathbf{z}}_\tau)]\Big|_{\tau=0} = b_N^*(^{n+1}\mathbf{z}; \Delta\dot{\mathbf{z}}, \bar{\mathbf{z}}) + b_N'(^{n+1}\mathbf{z}, \bar{\mathbf{z}}) \quad (34)$$

where

$$\begin{aligned} b_N^*(^{n+1}\mathbf{z}; \Delta\dot{\mathbf{z}}, \bar{\mathbf{z}}) &= \omega_n \int_{\Gamma_c} \hat{\mathbf{z}} \cdot \mathbf{nn} \cdot \Delta\dot{\mathbf{z}} d\Gamma - \omega_n \int_{\Gamma_c} g[\mathbf{n} \cdot \bar{\mathbf{z}}_{,\alpha} \dot{\xi}_\alpha(\Delta\dot{\mathbf{z}}) + \mathbf{n} \cdot \Delta\dot{\mathbf{z}}_{,\alpha} \bar{\xi}_\alpha \\ &\quad + \mathbf{n} \cdot {}^{n+1}\mathbf{x}_{,\alpha\beta}^c \bar{\xi}_\alpha \dot{\xi}_\beta(\Delta\dot{\mathbf{z}})] d\Gamma + \omega_n \int_{\Gamma_c} g^2[(\mathbf{n} \cdot \mathbf{e}_\alpha(\Delta\dot{\mathbf{z}})) m_{\alpha\beta}^{-1} (\mathbf{n} \cdot \bar{\mathbf{e}}_\beta)] d\Gamma \end{aligned} \quad (35)$$

is the same form as the linearization of the contact variational form in Equation (17) if we substitute $\Delta\mathbf{z}^k$ for $\Delta\dot{\mathbf{z}}$. This linearized form is used in the incremental equation (20) of the governing variational equation (18). The second term on the right of Equation (34) is the fictitious load form, for the problem with frictionless contact, which is defined as

$$b_N'(^{n+1}\mathbf{z}, \bar{\mathbf{z}}) \equiv b_N^*(^{n+1}\mathbf{z}; {}^n\mathbf{V}, \bar{\mathbf{z}}) + \omega_n \int_{\Gamma_c} [\kappa g \bar{\mathbf{z}} \cdot \mathbf{n} {}^n\mathbf{V}_n] d\Gamma \quad (36)$$

5. FRICTIONAL CONTACT DESIGN SENSITIVITY ANALYSIS

When friction exists on the contact surface, the structure experiences a tangential frictional force, in addition to the normal contact force. Since the frictional behaviour is complicated, many idealizations have been made. The Coulomb friction law is one of the frequently used methods to describe the frictional behaviour. However, this method presents numerical difficulties because of a discontinuity of the frictional force. A more advanced friction model assumes that the frictional force elastically increases until it reaches the limit value, and then the macroscopic slip occurs along the contact surface. This model is based on the experimental observation and corresponds to the non-associative flow rule in elastoplasticity. Thus, the return-mapping algorithm can be used to determine the frictional force similar to the elastoplasticity case.

5.1. Frictional model

The frictional force appears parallel to the contact surface and is expressed as

$$\mathbf{f} = f_\alpha \mathbf{e}^\alpha \quad (37)$$

where \mathbf{e}^α is the dual basis of \mathbf{e}_α and has the following relation:

$$\begin{aligned} \mathbf{e}^\alpha \cdot \mathbf{e}_\beta &= \delta_{\alpha\beta} \\ \mathbf{e}^\alpha &= m_{\alpha\beta}^{-1} \mathbf{e}_\beta \end{aligned} \quad (38)$$

where $m_{\alpha\beta} = \mathbf{e}_\alpha \cdot \mathbf{e}_\beta$ and $\delta_{\alpha\beta}$ is the Kronecker delta symbol, i.e. having a value of one when $\alpha = \beta$, and otherwise remaining at zero. The frictional contact form of the problem can then be defined by multiplying the frictional force by the virtual relative slip as

$$b_\Gamma(\mathbf{z}, \bar{\mathbf{z}}) = \int_{\Gamma^c} f_\alpha \bar{\xi}_\alpha \, d\Gamma \quad (39)$$

The expression $\bar{\xi}_\alpha$ can be obtained from the consistency condition in Equation (13) as

$$\bar{\xi}_\beta = A_{\alpha\beta}^{-1} (\hat{\bar{\mathbf{z}}} \cdot \mathbf{e}_\alpha + \mathbf{g}_n \cdot \bar{\mathbf{z}}_{,\alpha}) \quad (40)$$

In the regularized frictional model, frictional force f_α is calculated by using a return-mapping algorithm similar to the elastoplasticity case. Initially, the frictional force increases in proportion to the relative slip amount. This trial frictional force is then compared with the limit value $\mu\omega_N g$, where μ is Coulomb friction coefficient. If the trial force is smaller than the limit value, then the trial force becomes the frictional force (stick condition). If the trial force is greater than the limit value, then the limit value is used for the frictional force (slip condition). Figure 6 shows the frictional force used in this paper.

Similar to the frictionless contact form, the non-linear frictional contact form in Equation (39) has to be linearized as part of the implicit solution process. The linearized frictional contact form is denoted by $b_\Gamma^*(\mathbf{z}; \Delta\mathbf{z}, \bar{\mathbf{z}})$, whose expression is derived in the following section. If the following notations are used:

$$\begin{aligned} b_\Gamma^{(n+1)}(\mathbf{z}, \bar{\mathbf{z}}) &= b_N^{(n+1)}(\mathbf{z}, \bar{\mathbf{z}}) + b_T^{(n+1)}(\mathbf{z}, \bar{\mathbf{z}}) \\ b_\Gamma^*(\mathbf{z}; \Delta\mathbf{z}, \bar{\mathbf{z}}) &= b_N^*(\mathbf{z}; \Delta\mathbf{z}, \bar{\mathbf{z}}) + b_T^*(\mathbf{z}; \Delta\mathbf{z}, \bar{\mathbf{z}}) \end{aligned} \quad (41)$$

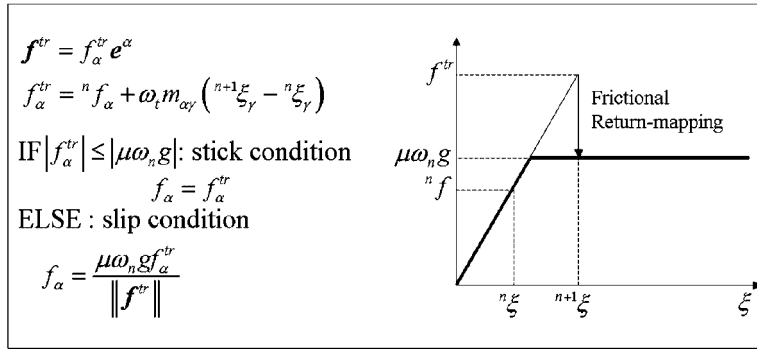


Figure 6. Return-mapping algorithm for frictional force.

then the linearized incremental equation can be extended to the frictional contact problem as

$$a_{\Omega}^*({}^{n+1} \mathbf{z}^k; \Delta \mathbf{z}^{k+1}, \bar{\mathbf{z}}) + b_{\Gamma}^*({}^{n+1} \mathbf{z}^k; \Delta \mathbf{z}^{k+1}, \bar{\mathbf{z}}) = \ell_{\Omega}(\bar{\mathbf{z}}) - a_{\Omega}({}^{n+1} \mathbf{z}^k, \bar{\mathbf{z}}) - b_{\Gamma}({}^{n+1} \mathbf{z}^k, \bar{\mathbf{z}}) \quad \forall \bar{\mathbf{z}} \in Z \quad (42)$$

It is shown in the next section that the same left-hand side of Equation (42) can be used in DSA. Also, the linearized frictional contact form $b_{\Gamma}^*({}^{n+1} \mathbf{z}; \bullet, \bar{\mathbf{z}})$ in Equation (41) will be derived during the process of design sensitivity formulation of the friction form in next section.

5.2. Design sensitivity formulation of friction form

Unlike the frictionless contact form, the frictional contact form depends on analysis results at the previous load step because of the updating algorithm of the frictional force. Thus, the sensitivity equation constitutes three parts: implicitly dependent terms, explicitly dependent terms, and path-dependent terms. The material derivative of the frictional contact form can be obtained from Equation (39) as

$$\frac{d}{d\tau} [b_{\Gamma}({}^{n+1} \mathbf{z}, \bar{\mathbf{z}})] \Big|_{\tau=0} = \int_{\Gamma^c} (f_{\alpha} \dot{\xi}_{\alpha} + f_{\alpha} \dot{\xi}_{\alpha} + \kappa f_{\alpha} \dot{\xi}_{\alpha}^n \mathbf{V}) d\Gamma \quad (43)$$

The material derivative of $\bar{\xi}_{\beta}$ can be obtained from Equation (40) as

$$A_{\alpha\beta} \dot{\xi}_{\beta} = -\mathbf{e}_{\alpha} \cdot \bar{\mathbf{z}}_{,\gamma} \dot{\xi}_{\gamma} + \hat{\mathbf{z}} \cdot \dot{\mathbf{e}}_{\alpha} + \bar{\mathbf{e}}_{\alpha} \cdot \Delta \hat{\mathbf{z}} - \bar{\mathbf{e}}_{\alpha} \cdot \mathbf{e}_{\beta} \dot{\xi}_{\beta} - \dot{\mathbf{e}}_{\alpha} \cdot \mathbf{e}_{\beta} \bar{\xi}_{\beta} - [\mathbf{e}_{\alpha} \cdot \mathbf{x}_{,\gamma\beta}^c - g \mathbf{n} \cdot \mathbf{x}_{,\alpha\gamma}^c] \dot{\xi}_{\beta} \bar{\xi}_{\gamma} - \mathbf{e}_{\alpha} \cdot \Delta \dot{\mathbf{z}}_{,\beta}^c \bar{\xi}_{\gamma} + g \mathbf{n} \cdot \Delta \dot{\mathbf{z}}_{,\alpha\gamma}^c \bar{\xi}_{\gamma} + g \mathbf{n} \cdot \bar{\mathbf{z}}_{,\alpha\beta}^c \dot{\xi}_{\beta} + \bar{\mathbf{e}}_{\alpha} \cdot {}^n \hat{\mathbf{V}} - \mathbf{e}_{\alpha} \cdot {}^n \mathbf{V}_{,\beta}^c \bar{\xi}_{\gamma} + g \mathbf{n} \cdot {}^n \mathbf{V}_{,\alpha\gamma}^c \bar{\xi}_{\gamma} \quad (44)$$

Note that Equation (44) includes the implicitly dependent ($\Delta \hat{\mathbf{z}}$) and the explicitly dependent term (${}^n \mathbf{V}$). No path-dependent term exists, and the expression is the same for both stick and slip conditions.

For the stick condition, the traction force increases in proportion to the amount of relative slip between two contact surfaces. The material derivative of the frictional force in Equation (37) becomes

$${}^{n+1} \dot{f}_{\alpha} = \omega_t \Phi_{\alpha\beta} \dot{\xi}_{\beta} (\Delta \hat{\mathbf{z}}) + \omega_t [\mathbf{e}_{\beta} \cdot \Delta \dot{\mathbf{z}}_{,\alpha}^c + \mathbf{e}_{\alpha} \cdot \Delta \dot{\mathbf{z}}_{,\beta}^c] ({}^{n+1} \xi_{\beta} - {}^n \xi_{\beta}) + \omega_t \Phi_{\alpha\beta} \dot{\xi}_{\beta} ({}^n \mathbf{V}) + \omega_t [\mathbf{e}_{\beta} \cdot {}^n \mathbf{V}_{,\alpha}^c + \mathbf{e}_{\alpha} \cdot {}^n \mathbf{V}_{,\beta}^c] ({}^{n+1} \xi_{\beta} - {}^n \xi_{\beta}) + {}^n \dot{f}_{\alpha} + \omega_t m_{\alpha\beta} \dot{\xi}_{\beta} \quad (45)$$

where $\Phi_{\alpha\beta} \equiv \omega_t\{[\mathbf{x}_{,\alpha\beta}^c \cdot \mathbf{e}_\gamma + \mathbf{e}_\alpha \cdot \mathbf{x}_{,\gamma\beta}^c](^{n+1}\xi_\gamma - ^n\xi_\gamma) + m_{\alpha\beta}\}$. In Equation (45), first and second terms on the right represent the implicitly dependent terms, third and fourth terms represent the explicitly dependent terms, and fifth and sixth terms represent the path-dependent terms.

By substituting Equations (44) and (45) into Equation (43), the material derivative of the frictional contact form is explicitly obtained in terms of $\Delta\dot{\mathbf{z}}$, ${}^n\mathbf{V}$, and the path-dependent terms, as

$$\left. \frac{d}{d\tau} [b_T(^{n+1}\mathbf{z}, \bar{\mathbf{z}})] \right|_{\tau=0} \equiv b_T^*(^{n+1}\mathbf{z}; \Delta\dot{\mathbf{z}}, \bar{\mathbf{z}}) + b_T'(^{n+1}\mathbf{z}, \bar{\mathbf{z}}) \tag{46}$$

where the linearized friction form is defined by collecting all terms that include $\Delta\dot{\mathbf{z}}$ as

$$\begin{aligned} b_T^*(^{n+1}\mathbf{z}; \Delta\dot{\mathbf{z}}, \bar{\mathbf{z}}) = & \int_{\Gamma^c} \{ \omega_t \Phi_{\alpha\beta} \xi_\beta (\Delta\dot{\mathbf{z}}) \bar{\xi}_\alpha + \omega_t [\Delta\dot{\mathbf{z}}_{,\alpha}^c \cdot \mathbf{e}_\beta + \mathbf{e}_\alpha \cdot \Delta\dot{\mathbf{z}}_{,\beta}^c] (^{n+1}\xi_\beta - ^n\xi_\beta) \bar{\xi}_\alpha \\ & + f_\alpha A_{\alpha\beta}^{-1} (-\mathbf{e}_\alpha \cdot \bar{\mathbf{z}}_{,\gamma}^c \xi_\gamma (\Delta\dot{\mathbf{z}}) + \hat{\mathbf{z}} \cdot \mathbf{e}_\alpha (\Delta\dot{\mathbf{z}}) + \bar{\mathbf{e}}_\alpha \cdot \Delta\dot{\mathbf{z}} - \bar{\mathbf{e}}_\alpha \cdot \mathbf{e}_\beta \xi_\beta (\Delta\dot{\mathbf{z}}) \\ & + \mathbf{e}_\alpha (\Delta\dot{\mathbf{z}}) \cdot \mathbf{e}_\beta \bar{\xi}_\beta + g \mathbf{n} \cdot \bar{\mathbf{z}}_{,\alpha\beta}^c \xi_\beta (\Delta\dot{\mathbf{z}}) - [\mathbf{e}_\alpha \cdot \mathbf{x}_{,\gamma\beta}^c - g \mathbf{n} \cdot \mathbf{x}_{,\alpha\gamma\beta}^c] \xi_\beta (\Delta\dot{\mathbf{z}}) \bar{\xi}_\gamma \\ & - \mathbf{e}_\alpha \cdot \Delta\dot{\mathbf{z}}_{,\beta}^c \bar{\xi}_\gamma + g \mathbf{n} \cdot \Delta\dot{\mathbf{z}}_{,\alpha\gamma}^c \bar{\xi}_\gamma \gamma \} d\Gamma \end{aligned} \tag{47}$$

and the fictitious load form due to friction is obtained by collecting those explicitly dependent terms and path-dependent terms as

$$b_T'(^{n+1}\mathbf{z}, \bar{\mathbf{z}}) = b_T^*(^{n+1}\mathbf{z}; {}^n\mathbf{V}, \bar{\mathbf{z}}) + \int_{\Gamma^c} \kappa f_\alpha \bar{\xi}_\alpha {}^n\mathbf{V} d\Gamma + \int_{\Gamma^c} ({}^n \dot{f}_\alpha \bar{\xi}_\alpha + \omega_t m_{\alpha\beta} \bar{\xi}_\alpha {}^n \dot{\xi}_\beta) d\Gamma \tag{48}$$

For the slip condition, the magnitude of the frictional force is determined from the normal contact force, while the applied direction is parallel to the trial force. From the return-mapping algorithm given in Figure 6, the material derivative of the frictional force for the slip condition is obtained as

$${}^{n+1} \dot{f}_\alpha = \mu \omega_n p_\alpha \mathbf{n} \cdot (\Delta\dot{\mathbf{z}} + {}^n\hat{\mathbf{V}}) + \frac{\mu \omega_n g}{\|\mathbf{f}^{tr}\|} [f_\alpha^{tr} - p_\alpha p^\beta f_\beta^{tr} - f_\alpha^{tr} p_\beta \mathbf{p} \cdot \mathbf{e}^\beta] \tag{49}$$

where $\mathbf{p} = \mathbf{f}^{tr} / \|\mathbf{f}^{tr}\|$, $p_\alpha = f_\alpha^{tr} / \|\mathbf{f}^{tr}\|$, and $p^\beta = \mathbf{p} \cdot \mathbf{e}^\beta$. In Equation (49), f_α^{tr} is the same as in Equation (45) for the stick condition. By substituting Equations (44) and (49) into Equation (43), the material derivative of the frictional contact form is obtained. If the implicitly dependent terms are combined, the linearized frictional contact form can be obtained as

$$\begin{aligned} b_T^*(^{n+1}\mathbf{z}; \Delta\dot{\mathbf{z}}, \bar{\mathbf{z}}) = & \mu \omega_n \int_{\Gamma^c} \{ p_\alpha \bar{\xi}_\alpha \mathbf{n} \cdot \Delta\dot{\mathbf{z}} + \omega_t g (\delta_{\alpha\beta} - p_\alpha p^\beta) / \|\mathbf{f}^{tr}\| [\Phi_{\beta\gamma} \xi_\gamma (\Delta\dot{\mathbf{z}}) \\ & + \omega_t [\mathbf{e}_\beta \cdot \Delta\dot{\mathbf{z}}_{,\gamma}^c + \Delta\dot{\mathbf{z}}_{,\beta}^c \cdot \mathbf{e}_\gamma] (^{n+1}\xi_\gamma - ^n\xi_\gamma) \bar{\xi}_\alpha \} d\Gamma \\ & - \mu \omega_n \int_{\Gamma^c} \{ g p_\alpha p^\beta \bar{\xi}_\alpha \{ [\mathbf{p} \cdot \mathbf{x}_{,\beta\gamma}^c - ([\mathbf{x}_{,\beta\gamma}^c \cdot \mathbf{e}_\phi + \mathbf{e}_\beta \cdot \mathbf{x}_{,\phi\gamma}^c] \mathbf{p} \cdot \mathbf{e}^\phi)] \xi_\gamma (\Delta\dot{\mathbf{z}}) \} \end{aligned}$$

$$\begin{aligned}
 &+ \mathbf{p} \cdot \Delta \dot{\mathbf{z}}_{,\beta}^c - (\Delta \dot{\mathbf{z}}_{,\beta}^c \cdot \mathbf{e}_\gamma + \Delta \dot{\mathbf{z}}_{,\gamma}^c \cdot \mathbf{e}_\beta) \mathbf{p} \cdot \mathbf{e}^\gamma \} d\Gamma \\
 &+ \int_{\Gamma^c} \{ f_\alpha A_{\alpha\beta}^{-1} (-\mathbf{e}_\alpha \cdot \bar{\mathbf{z}}_{,\gamma}^c \xi_\gamma(\Delta \dot{\mathbf{z}}) + \hat{\mathbf{z}} \cdot \mathbf{e}_\alpha(\Delta \dot{\mathbf{z}}) + \bar{\mathbf{e}}_\alpha \cdot \Delta \hat{\mathbf{z}} - \bar{\mathbf{e}}_\alpha \cdot \mathbf{e}_\beta \xi_\beta(\Delta \dot{\mathbf{z}}) \\
 &+ \mathbf{e}_\alpha(\Delta \dot{\mathbf{z}}) \cdot \mathbf{e}_\beta \bar{\xi}_\beta + \mathbf{g}_n \cdot \bar{\mathbf{z}}_{,\alpha\beta}^c \xi_\beta(\Delta \dot{\mathbf{z}}) - \mathbf{e}_\alpha \cdot \Delta \dot{\mathbf{z}}_{,\beta}^c \bar{\xi}_\gamma + \mathbf{g}_n \cdot \Delta \dot{\mathbf{z}}_{,\alpha\gamma}^c \bar{\xi}_\gamma \\
 &- [\mathbf{e}_\alpha \cdot \mathbf{x}_{,\gamma\beta}^c - \mathbf{g}_n \cdot \mathbf{x}_{,\alpha\gamma\beta}^c] \xi_\beta(\Delta \dot{\mathbf{z}}) \bar{\xi}_\gamma \} d\Gamma \tag{50}
 \end{aligned}$$

In a similar way, the explicitly dependent terms and path-dependent terms are combined to define the fictitious load form due to friction as

$$\begin{aligned}
 b'_T(n+1, \mathbf{z}, \bar{\mathbf{z}}) &= b_T^*(n+1, \mathbf{z}^k; {}^n\mathbf{V}, \bar{\mathbf{z}}) + \int_{\Gamma^c} \kappa f_\alpha \bar{\xi}_\alpha {}^n\mathbf{V} d\Gamma \\
 &+ \int_{\Gamma^c} \frac{\mu \omega_n g}{\|\mathbf{f}^r\|} (\delta_{\alpha\beta} - p_\alpha p^\beta) ({}^n \dot{f}_\alpha + \omega_t m_{\alpha\beta} {}^n \dot{\xi}_\beta) \bar{\xi}_\alpha d\Gamma \tag{51}
 \end{aligned}$$

By adding Equations (36) and (48) for the stick condition, or Equations (36) and (51) for the slip condition, the total fictitious load from due to frictional contact can be defined as

$$b'_V(n+1, \mathbf{z}, \bar{\mathbf{z}}) \equiv b'_N(n+1, \mathbf{z}, \bar{\mathbf{z}}) + b'_T(n+1, \mathbf{z}, \bar{\mathbf{z}}) \tag{52}$$

Finally, by adding the material derivatives in Equations (25), (34), and (46), and using Equation (52), the design sensitivity equation for the frictional contact problem is obtained as

$$a_{\Omega}^*(n+1, \mathbf{z}; \Delta \dot{\mathbf{z}}, \bar{\mathbf{z}}) + b_{\Gamma}^*(n+1, \mathbf{z}; \Delta \dot{\mathbf{z}}, \bar{\mathbf{z}}) = \ell'_V(\bar{\mathbf{z}}) - a'_V(n+1, \mathbf{z}, \bar{\mathbf{z}}) - b'_V(n+1, \mathbf{z}, \bar{\mathbf{z}}) \quad \forall \bar{\mathbf{z}} \in Z \tag{53}$$

where

$$b_{\Gamma}^*(n+1, \mathbf{z}; \Delta \dot{\mathbf{z}}, \bar{\mathbf{z}}) \equiv b_N^*(n+1, \mathbf{z}; \Delta \dot{\mathbf{z}}, \bar{\mathbf{z}}) + b_T^*(n+1, \mathbf{z}; \Delta \dot{\mathbf{z}}, \bar{\mathbf{z}}) \tag{54}$$

Since the left-hand side of Equation (53) is same as the left-hand side of Equation (42) if $\Delta \dot{\mathbf{z}}$ is replaced by $\Delta \mathbf{z}^{k+1}$, the design sensitivity equation uses the same stiffness matrix as response analysis that already has a factorized form. This provides an excellent efficiency in computation of design sensitivity.

Figure 7 shows the flow chart of the response analysis and DSA. The response analysis of a stamping process involves elastoplasticity, finite deformation, and frictional contact of shell structure. For the response analysis of the finite deformation elastoplastic shell structure, which corresponds to $a_{\Omega}^*(n+1, \mathbf{z}^k; \Delta \mathbf{z}^{k+1}, \bar{\mathbf{z}})$ and $a_{\Omega}(n+1, \mathbf{z}^k, \bar{\mathbf{z}})$ in Equation (42), the Hughes–Winget’s incrementally objective integration with the elastoplastic return-mapping algorithm for the shell structure is used. The detail discussion of the response analysis and DSA using the meshfree method can be found in Yi *et al.* [23]. The non-linear response analysis is to find the equilibrium state corresponding to the applied loads. Time variable t is used to denote the intensities of load applications, or different punch location in a stamping process, and correspondingly different configurations. The basic approach in non-linear response analysis is to assume that the solution at time t is known and that the solution at time $t + \Delta t$ is required. That is, Equation (42) is solved iteratively to obtain the incremental displacement $\Delta \mathbf{z}$ based on the Newton–Raphson iteration method. After the

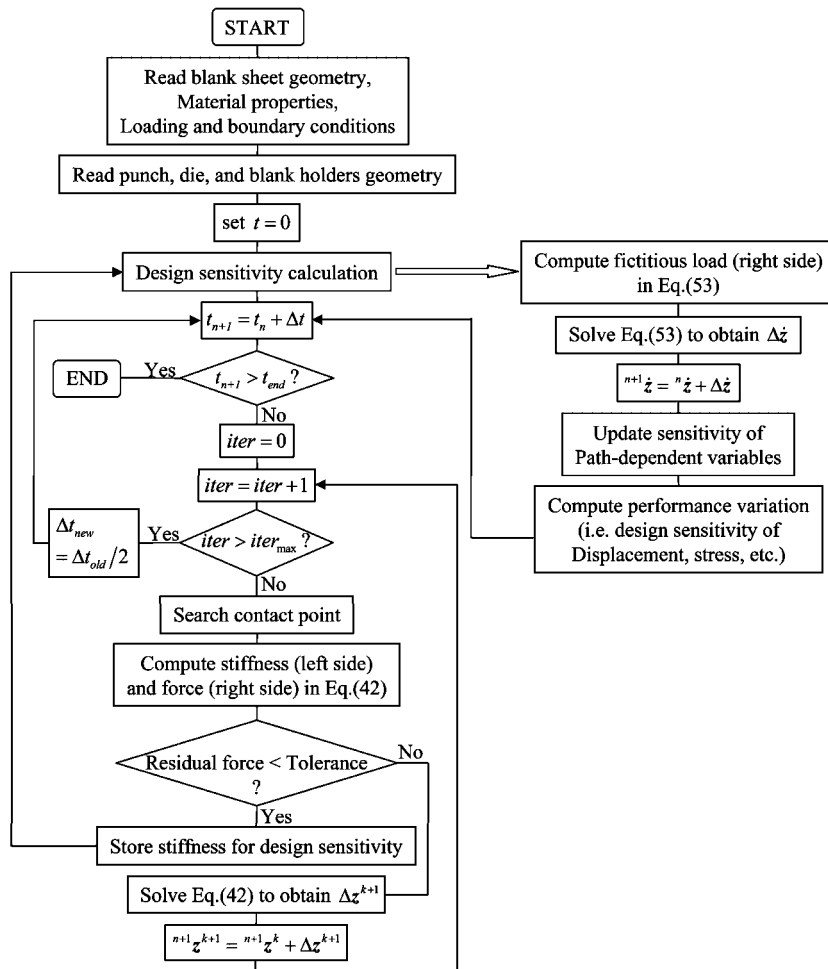


Figure 7. Flow chart of response analysis and design sensitivity analysis.

converged solution is obtained, Equation (53) is solved without iteration to calculate the design sensitivity of incremental displacement $\Delta \dot{z}$. In DSA, since the left-hand side of Equation (53) is same as that of (42), the sensitivity calculation is carried out without iteration, which makes DSA very efficient.

The sensitivity at the points of interests before springback is evaluated by simply summing design sensitivity of the incremental displacement up to before springback. Likewise, the sensitivity at the points of interests after springback is evaluated by simply summing design sensitivity of the incremental displacement up to after springback. For example, if 200 time steps are used for loading and 40 time steps are used for unloading, summing sensitivity of incremental displacement from the first to the 200th time step will give sensitivity before springback, and summing from the first to the 240th time step will give sensitivity after springback.

6. NUMERICAL EXAMPLES

Two numerical example problems are used in this section to demonstrate accuracy and efficiency of the proposed DSA method and its application to optimization of metal stamping process for the springback problem.

6.1. Design sensitivity analysis of deep drawing problem

In deep drawing problem, a sheet of metal is clamped by a constant blank-holding force between the blank holder and die, and then subjected to bending by the punch as shown in Figure 8, which shows half of the model using symmetry. The final shape after unloading is sought to compute the springback. This problem is one of the benchmark problems of NUMISHEET'93 and considered in this section to verify the proposed continuum-based DSA method. The springback in this problem is expected to be very large. A total of 205 meshfree particles are used. A 2.45 kN blank-holding force is used. Due to symmetry, a half of deep drawing is modelled. The dimensions of blank sheet are 175 mm(L) \times 17.5 mm(W) \times 0.78 mm(t). The total punch stroke is 70 mm. The material properties are Young's modulus $E = 206$ GPa, Poisson ratio $\nu = 0.3$, yielding strength $\sigma_Y = 167$ MPa, and the hardening slope $H = 20$ GPa.

The frictional contact constraints are imposed between the blank metal sheet and rigid punch and die with a friction coefficient of $\mu = 0.14$. Symmetric boundary condition is imposed at the end of the blank sheet metal that contacts punch. The non-linear response analysis is carried out with 200 loading steps and 40 unloading steps, respectively. The computed unloading shape (springback) is shown in Figure 9.

DSA is carried out using design parameters, which are illustrated in Figure 10: u_1 and u_2 are the horizontal and vertical locations of the punch, respectively, u_3 and u_6 are the punch and die corner radii, respectively, u_4 and u_5 are the horizontal and vertical locations of the die, respectively, and u_7 is the blank-holding force. In case u_1 and u_4 are changed the same amount, then the gap

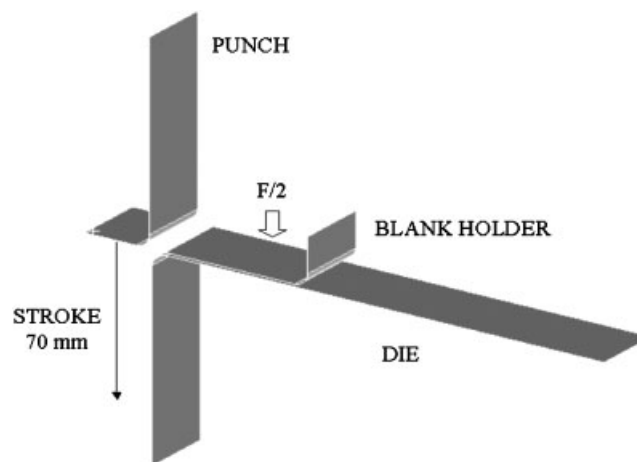


Figure 8. Schematic diagram of deep drawing problem.

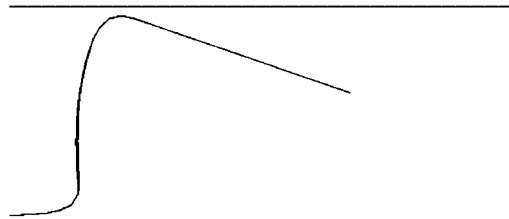


Figure 9. Result of deep drawing problem analysis.

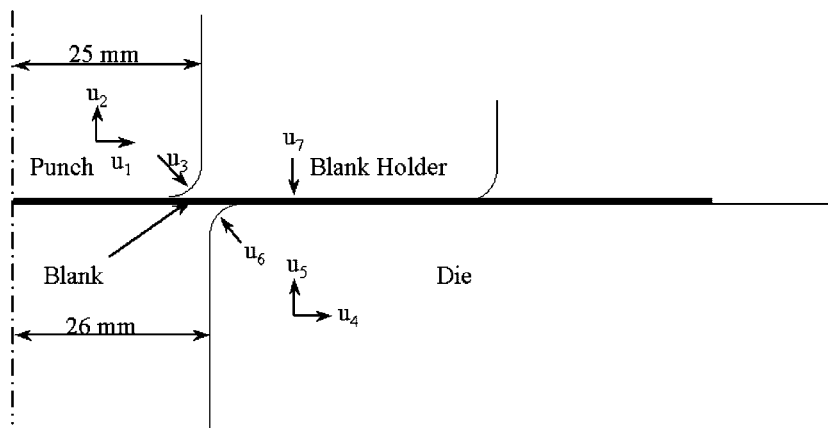


Figure 10. Shape and configuration design parameters for deep drawing problem.

between punch and die remains same. However, this would change the width of punch. Therefore, u_1 and u_4 are defined independently. Also, if u_2 and u_5 are changed the same amount, then the vertical gap between punch and die remains the same. But, this would change the distance between the blank holder and die as well as the total punch stroke. Therefore, u_2 and u_5 are defined independently. The non-linear DSA is carried out at each converged load steps to compute the material derivative of the displacement with the same tangent stiffness matrix as the response analysis without iteration. The vertical displacement sensitivity results at randomly selected blank location after unloading are compared with the finite difference results in Table I. The first column denotes the design variable ID; the second column denotes the performance measure, which is the vertical displacement; the third column denotes the performance value; the fourth column denotes the perturbed result from FDM; the fifth column denotes the prediction from the calculated sensitivity results; and the last column compares the results between the fourth and fifth columns. The sensitivity results are very well matched with the finite difference results. The response analysis is carried out in 12 314 s, whereas DSA in 987 s per design variable, which means that the cost of sensitivity computation is only 8% of the response analysis time (or FDM computation time), which is quite efficient compared to the finite difference method.

Table I. Accuracy of sensitivity analysis results of deep drawing.

Design variable	Performance measure (vertical displacement at randomly selected point)	Performance ψ	FDM $\Delta\psi$ (it took 12 314 s per design variable)	Calculated sensitivity $\psi' \times \Delta\tau$ (it took 987 s per design variable)	Difference between FDM and calculated sensitivity $((\Delta\psi - \psi' \times \Delta\tau) / \psi' \times \Delta\tau) \times 100$
u_1	z_{99}	-1.93126E - 02	-3.24044E - 10	-3.24054E - 10	0.00
	z_{104}	-2.10971E - 03	5.77483E - 10	5.77540E - 10	-0.01
	z_{115}	-1.29131E - 02	1.23001E - 09	1.23006E - 09	0.00
	z_{123}	-2.11297E - 02	1.62901E - 09	1.62906E - 09	0.00
u_2	z_{99}	-1.93126E - 02	8.99570E - 10	8.99603E - 10	0.00
	z_{104}	-2.10971E - 03	-1.02359E - 10	-1.02251E - 10	0.00
	z_{115}	-1.29131E - 02	-1.49452E - 10	-1.49155E - 10	0.20
	z_{123}	-2.11297E - 02	1.05384E - 10	1.05834E - 10	-0.42
u_3	z_{99}	-1.93126E - 02	5.67422E - 10	5.67422E - 10	-0.02
	z_{104}	-2.10971E - 03	-4.00822E - 11	-3.97581E - 11	0.82
	z_{115}	-1.29131E - 02	-6.65856E - 11	-6.62435E - 11	0.52
	z_{123}	-2.11297E - 02	9.15206E - 11	9.19059E - 11	-0.42
u_4	z_{99}	-1.93126E - 02	1.00422E - 10	1.00397E - 10	0.02
	z_{104}	-2.10971E - 03	1.10236E - 09	1.10225E - 09	0.01
	z_{115}	-1.29131E - 02	1.14945E - 09	1.14915E - 09	0.03
	z_{123}	-2.11297E - 02	8.94604E - 10	8.94165E - 10	0.05
u_5	z_{99}	-1.93126E - 02	-5.23843E - 10	-5.23876E - 10	-0.01
	z_{104}	-2.10971E - 03	-2.94645E - 10	-2.94821E - 10	-0.06
	z_{115}	-1.29131E - 02	-8.39441E - 10	-8.39846E - 10	-0.05
	z_{123}	-2.11297E - 02	-1.46829E - 09	-1.46887E - 09	-0.04
u_6	z_{99}	-1.93126E - 02	-3.08749E - 10	-3.08716E - 10	0.01
	z_{104}	-2.10971E - 03	-9.20905E - 10	-9.21081E - 10	-0.02
	z_{115}	-1.29131E - 02	-1.98298E - 09	-1.98324E - 09	-0.01
	z_{123}	-2.11297E - 02	-2.95603E - 09	-2.95635E - 09	-0.01
u_7	z_{99}	-1.93126E - 02	2.11959E - 13	2.15909E - 13	1.19
	z_{104}	-2.10971E - 03	-4.63656E - 13	-4.63121E - 13	0.12
	z_{115}	-1.29131E - 02	-8.10140E - 13	-8.07624E - 13	0.31
	z_{123}	-2.11297E - 02	-9.13079E - 13	-9.08616E - 13	0.49

6.2. Optimization of metal stamping process for springback problem

The S-rail benchmark problem of NUMISHEET'96 is selected in this paper to demonstrate the efficiency and effectiveness of the proposed method for a stamping process optimization. This is a challenging problem, even for accuracy of the analysis, let alone for DSA and optimization.

The blank sheet with thickness $t = 0.92$ mm is placed on the die and hold by the blank holder with constant force 10 kN. Then, the punch is pressed down with 37 mm stroke and removed. Due to elasticity, significant springback occurs. The material properties are Young's modulus $E = 69$ GPa,

Poisson ratio $\nu=0.33$, and the yield strength $\sigma_Y=241$ MPa. For elastoplasticity, the combined linear isotropic–kinematic hardening rule is used with a hardening slope of $H=200$ MPa. The modified Coulomb friction law is used with a friction coefficient of 0.1. Figure 11 shows the tool surfaces for the S-rail forming process and Figure 12 shows the blank sheet. As stated in

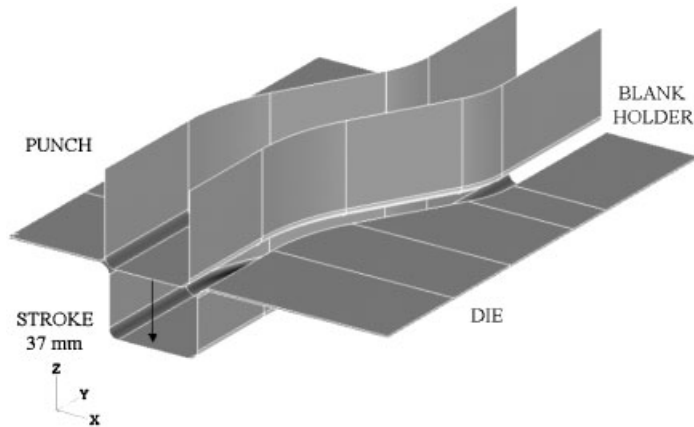


Figure 11. Schematic diagram of S-rail forming and springback.

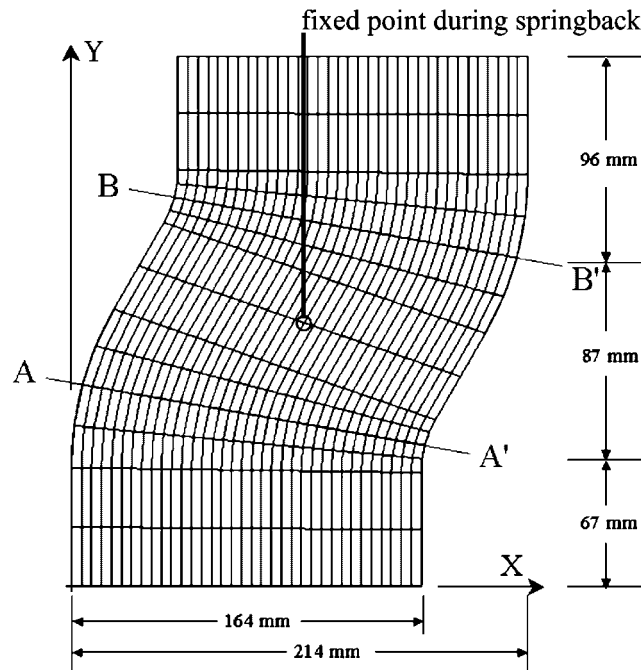


Figure 12. Blank sheet of S-rail forming and springback.

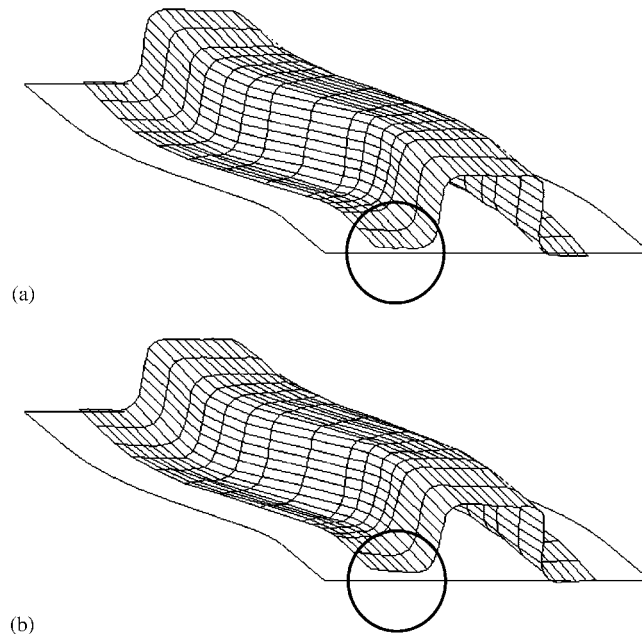


Figure 13. Deformed shape: (a) before springback and (b) after springback.

Introduction, the numerical implementation of the non-linear analysis DSA is carried out using the meshfree method. Since no element information is available in the meshfree method, FE mesh is used to represent results. Each FE node is selected as the meshfree particle.

Since the die, punch, and blank holder are rigid, only blank sheet is discretized using 540 meshfree particles. In addition, the vertical displacement of the blank holder needs to be computed. Therefore, 2701 degrees-of-freedom are used to model the stamping process. The order of the meshfree shape function is much higher than FEA. Therefore, the springback deformation can be simulated better than FEA even with rather coarse meshfree particles. Two hundred time steps have been used to carry out the non-linear analysis, which took 39 908 s using a workstation with 1 GHz Itanium CPU. Figures 13(a) and (b) show deformed shapes before and after springback. In order to calculate the deformed shape after the tools are removed, one point is fixed to avoid rigid-body motion as shown in Figure 12. Since each point in shell formulation has translation and rotation degree-of-freedom, fixing one point is enough to avoid rigid-body motion. Fixing more than one point results in unnecessary constraint on unloading (when the tools are removed) deformation, thus the unloading deformation will be different for different fixing point. Even in the case when only one point is fixed during unloading, the deformed shape after springback depends on the location of the fixing point. For example, different fixing point will yield different unloading deformation. However, those different unloading deformations can be identical by rigid-body translation and rotation. Therefore, the choice of the fixing point location is not critical to the optimal solution. The same point is fixed throughout the optimization iterations. The deformed shape along the line $A-A'$ on Figure 12 is shown in Figure 14, where significant springback has occurred. Thus, stamping process optimization is carried out to minimize the springback. In this example, the die

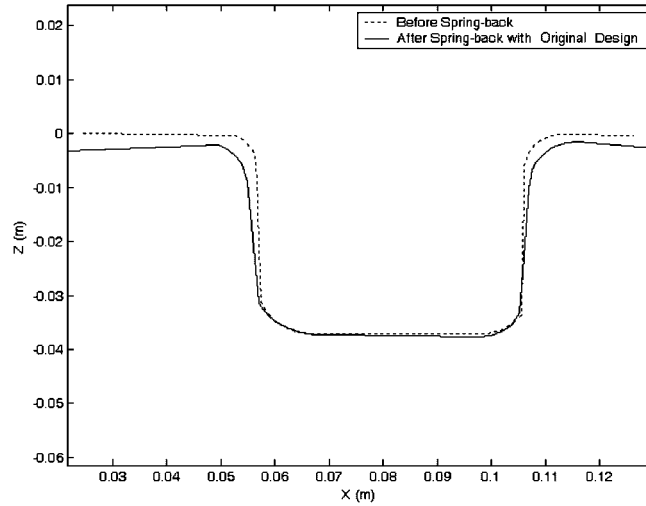


Figure 14. Deformed shape along line A–A' before and after springback.

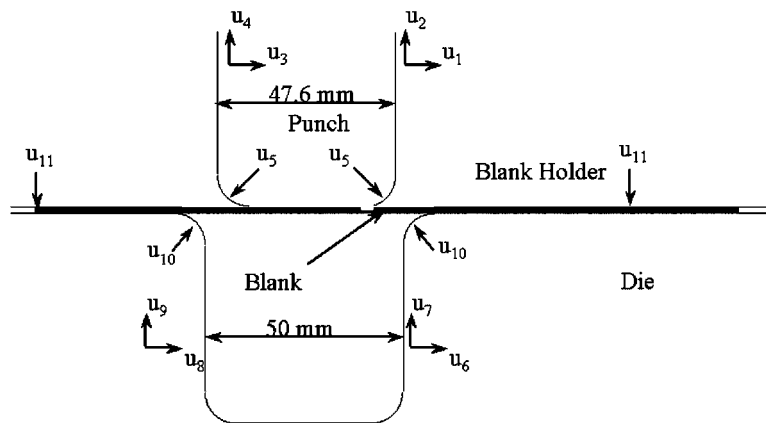


Figure 15. Shape and configuration parameters for S-rail stamping process.

and punch cross-section shapes are assumed to be constant along the S-lane. With this assumption, it is not viable to reduce the springback at the entire part. Therefore, one two-dimensional section (which is used to judge numerical simulation quality in NUMISHEET'96) is selected to reduce the springback.

The stamping parameters are defined as shown in Figure 15. The stamping parameters u_1 – u_4 represent the horizontal and vertical location of each side of punch and u_6 – u_9 represent those of die. The stamping parameters u_5 and u_{10} represent corner radius of punch and die, respectively. The stamping parameter u_{11} represents the blank-holding force. The computational time for the continuum-based DSA per each stamping parameter is 2113 s, which corresponds to 5.3% of the

Table II. Accuracy of design sensitivity results.

Performance measure (vertical displacement at randomly selected point)	Performance ψ	FDM $\Delta\psi$ (it took 39 908 s per design variable)	Calculated sensitivity $\psi' \times \Delta\tau$ (it took 2113 s per design variable)	Difference between FDM and calculated sensitivity $((\Delta\psi - \psi' \times \Delta\tau)/\psi' \times \Delta\tau) \times 100$
Z ₁₀₉	-1.3555E - 03	5.1913E - 10	5.1989E - 10	-0.15
Z ₁₁₄	-5.2567E - 03	-3.2754E - 09	-3.2873E - 09	-0.36
Z ₁₁₉	-2.8827E - 02	-3.2496E - 09	-3.2619E - 09	-0.38
Z ₁₂₂	-3.7159E - 02	4.4464E - 10	4.4617E - 10	-0.34
Z ₁₂₅	-3.6658E - 02	-3.2416E - 10	-3.2346E - 10	0.22
Z ₁₂₆	-3.7233E - 02	-5.0735E - 10	-5.0659E - 10	0.15
Z ₁₃₁	-3.1223E - 02	2.2928E - 09	2.3064E - 09	-0.59
Z ₁₃₃	-2.1987E - 02	2.2657E - 09	2.2798E - 09	-0.61
Z ₁₃₈	-9.0185E - 04	-2.4509E - 10	-2.4106E - 10	1.67
Z ₁₄₁	-6.2609E - 04	-1.1656E - 09	-1.1672E - 09	-0.14
Z ₁₄₂	-1.0870E - 03	-3.4639E - 10	-3.4813E - 10	-0.50
Z ₁₄₄	-1.3831E - 05	-1.5467E - 10	-1.5505E - 10	-0.24

response analysis time, and thus very efficient compared to the FDM. The accuracy of the sensitivity results of vertical displacements after springback along the lines $A-A'$ and $B-B'$ with respect to stamping parameter u_6 is compared with the finite difference results in Table II. Extremely accurate sensitivity results are obtained, as shown in Table II.

The optimization problem is formulated to minimize the springback by the following equations:

$$\begin{aligned}
 \min \quad & (z_{144}^{\text{before_sb}} - z_{144}^{\text{after_sb}}) \\
 \text{s.t.} \quad & (z_{109}^{\text{before_sb}} - z_{109}^{\text{after_sb}}) \leq 0.0015 \\
 & e^p \leq 0.2 \\
 & -0.1 \leq u_1 \leq 0.001 \\
 & -0.001 \leq u_{2-4} \leq 0.1 \\
 & -2.0 \leq u_5 \leq 2.0 \\
 & -0.001 \leq u_6 \leq 0.1 \\
 & -0.1 \leq u_{7-9} \leq 0.001 \\
 & -2.0 \leq u_{10-11} \leq 2.0
 \end{aligned} \tag{55}$$

The target shape is considered to be the deformed shape before unloading. The optimal shape is obtained to minimize the springback at the flange located at two top ends.

For optimization, the springback at flange is minimized. In (55), $z_{144}^{\text{before_sb}}$ and $z_{144}^{\text{after_sb}}$ are the vertical displacements at the left end of the blank sheet in Figure 14 before and after springback, respectively. Similarly, $z_{109}^{\text{before_sb}}$ and $z_{109}^{\text{after_sb}}$ are vertical displacements at the right end of the blank sheet before and after springback, respectively. The initial values of $(z_{144}^{\text{before_sb}} - z_{144}^{\text{after_sb}})$ and

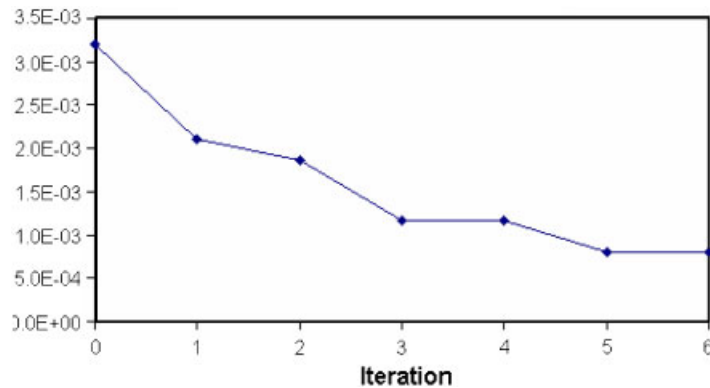


Figure 16. Cost function history of S-rail forming.

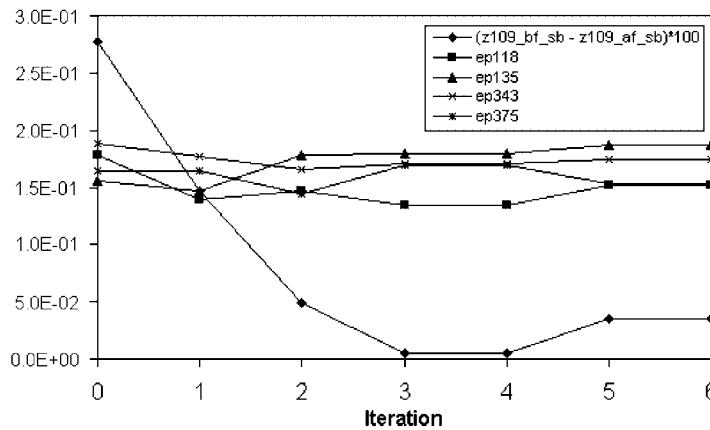


Figure 17. Constraint history of S-rail forming.

$(z_{109}^{\text{before_sb}} - z_{109}^{\text{before_sb}})$ are 3.2 and 2.7 mm, respectively. Thus, the first constraint, which is imposed on the amount of the springback at the right end of the blank sheet is violated significantly at the initial design of the manufacturing process. This optimization formulation was used, instead of trying to minimize the springback at both ends simultaneously, since it converged better in the optimization process. The effective plastic strain constraints are imposed to limit the amount that may result in material failure or severe necking. The maximum effective plastic strain at the initial stamping process is 0.188, which makes the initial stamping process satisfy the effective plastic strain constraints. Limits of stamping parameters are established according to work piece geometry and kinematics. Since the stamping parameters represent structure's relative movements, the initial values are set to zero.

The stamping process optimization problem is solved using the sequential linear programming method in DOT [33] by providing the meshfree analysis results and design sensitivity computed using the proposed method. As shown in Figure 16, the optimization problem is converged in six

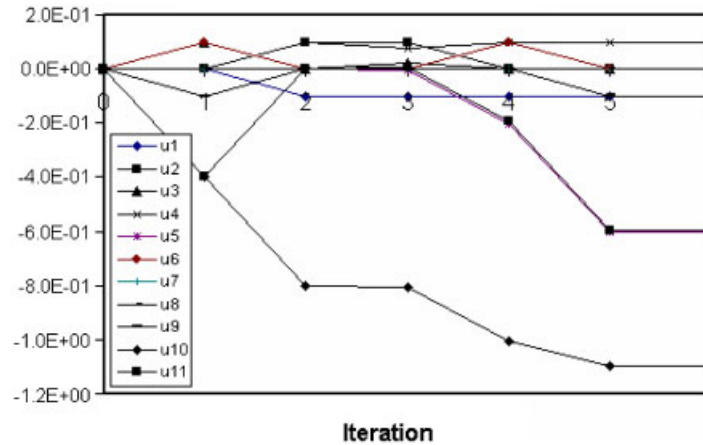


Figure 18. Design parameter history of S-rail forming.

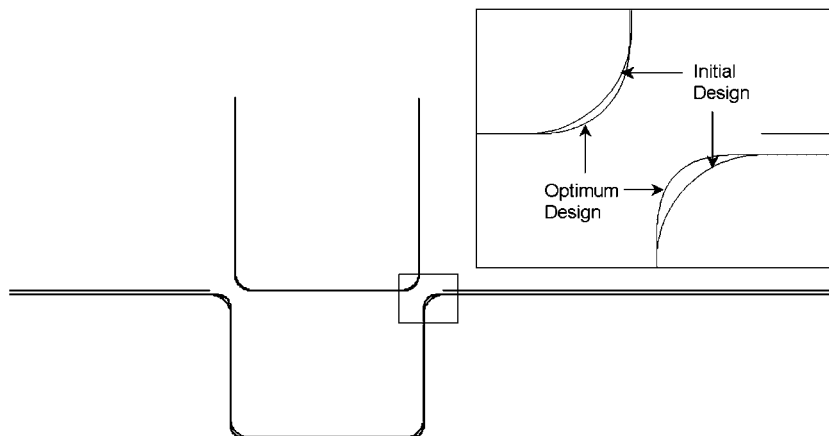


Figure 19. Punch and die shape of the initial and optimum design.

iterations, which is quite fast considering the degree of high non-linearity involved in the structural analysis. The cost function, which is the springback at the left end of the blank sheet, is reduced by 75% (from 3.2 to 0.8 mm) during the optimization. On the other hand, the springback at the right end of the blank sheet, which is the first constraint, is reduced significantly from 2.7 to 0.35 mm as shown in Figure 17. The effective plastic strain constraints are also satisfied. The design parameter history is given in Figure 18. The punch and die shape of the initial and optimum designs are shown in Figure 19. It is noticed that the corner radius of the die, u_{10} , and the corner radius of the punch, u_5 , are significantly reduced. It is also interesting to note that the blank-holding force, u_{11} , is decreased from the initial design, which in turn reduces the frictional force. Unlike some

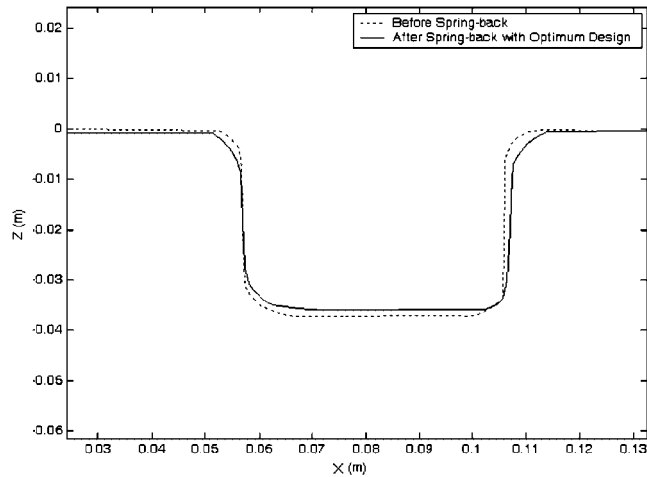


Figure 20. Deformed shape along $A-A'$ before and after springback of the optimum stamping process.

optimum design results of linear models, it is not easy to explain why these optimum stamping process parameters yield minimized springback.

The deformed shape for the optimum manufacturing process is shown in Figure 20. Over deflection of the initial stamping process around the blank holder area is significantly reduced in order to minimize the springback that is shown in Figure 14. The vertical slope is also improved as compared to the initial stamping process. By comparing the Figures 14 and 20, it can be noticed that the base of the deformed shape after springback in Figure 20 is higher than that in Figure 14. This is because the optimal design is obtained by minimizing the springback at flange located at two top ends. If the base of the deformed shape after springback is considered as one of design constraints, a different optimal design would be obtained. However, it was not easy to obtain optimal design that reduces the springback at every point with the limited manufacturing parameters. Thus, in this example, the springback at the flange is considered because it is assembled with the other part.

7. CONCLUSION

A continuum-based design sensitivity analysis (DSA) and optimization method for the stamping process has been developed. A penalty-regularized contact variational equation is differentiated with respect to the shape design parameter. A shape DSA is carried out by defining a design velocity field at the tool surface geometry. The material derivative concept is used to develop the continuum-based design sensitivity. Since the proposed DSA method uses the same tangent stiffness as the analysis at the converged configuration of each time step, no iteration is required to solve the sensitivity equation. Consequently, the proposed DSA takes much less computational time than finite difference method (FDM). For example, the proposed DSA takes only 8 and 5.3% of the FDM computational time for the deep drawing problem and S-rail benchmark problem, respectively. The sensitivity information is compared with finite difference results with excellent

agreement. The effectiveness of the proposed continuum-based DSA method is demonstrated through successful optimization of the benchmark S-rail stamping process, where the springback is significantly reduced by determining optimal tool shape and blank-holding force.

NOMENCLATURE

\mathbf{n}	surface normal vector
\mathbf{l}, \mathbf{m}	surface tangent vectors
\mathbf{J}	Jacobian matrix between the physical and parametric co-ordinate
J_1	Jacobian between configuration t_n and t_{n+1}
\mathbf{F}	deformation gradient matrix
\mathbf{z}	displacement field
$\Delta \mathbf{z}$	incremental displacement vector
$\bar{\mathbf{z}}$	virtual displacement
$\boldsymbol{\sigma}$	local Cauchy stress vector of dimension 5
$\boldsymbol{\sigma}^g$	global Cauchy stress vector of dimension 9
$\boldsymbol{\sigma}^l$	local Cauchy stress vector of dimension 9
\mathbf{s}	deviatoric Cauchy stress vector of dimension 5
$\boldsymbol{\varepsilon}$	local strain vector of dimension 5
$\boldsymbol{\varepsilon}^g$	global strain vector of dimension 9
$\boldsymbol{\varepsilon}^l$	local strain vector of dimension 9
$a^{(n+1)}(\mathbf{z}, \bar{\mathbf{z}})$	structural variational form
$a^{*(n+1)}(\mathbf{z}^k; \Delta \mathbf{z}^{k+1}, \bar{\mathbf{z}})$	linearized structural variational form
$a'_V{}^{(n+1)}(\mathbf{z}, \bar{\mathbf{z}})$	structural fictitious load form
$b_\Gamma{}^{(n+1)}(\mathbf{z}, \bar{\mathbf{z}})$	contact variational form
$b_N{}^{(n+1)}(\mathbf{z}, \bar{\mathbf{z}})$	normal contact variational form
$b_T{}^{(n+1)}(\mathbf{z}, \bar{\mathbf{z}})$	tangential slip variational form
$b_\Gamma^{*(n+1)}(\mathbf{z}^k; \Delta \mathbf{z}^{k+1}, \bar{\mathbf{z}})$	linearized contact variational form
$b'_V{}^{(n+1)}(\mathbf{z}, \bar{\mathbf{z}})$	contact fictitious load form
$\ell(\bar{\mathbf{z}})$	external load form
$\ell'_V{}(\bar{\mathbf{z}})$	external fictitious load form
${}^n \mathbf{V}$	design velocity field at time t_n
\mathbf{G}	surface geometric matrix
$C(\boldsymbol{\xi}; \boldsymbol{\xi} - \boldsymbol{\xi}_I)$	correction function
$\phi_a(\boldsymbol{\xi} - \boldsymbol{\xi}_I)$	kernel function
Ψ_I	meshfree shape function at particle I
$\boldsymbol{\alpha}$	back stress
$\boldsymbol{\alpha}'$	deviatoric back stress
$\bar{\varepsilon}^P$	effective plastic strain
$\kappa(\bar{\varepsilon}^P)$	radius of the yield surface
H	hardening parameter
f	yield function
$\bar{\mathbf{P}}$	mapping matrix between Cauchy stress and deviatoric Cauchy stress

P	mapping matrix modified from $\bar{\mathbf{P}}$ in order to account for the factor of two in the shear strain component
Z	space of kinematically admissible virtual displacement
${}^{n+1}\mathbf{Q}$	global-to-local transformation matrix at configuration t_{n+1}
D	elastic constitutive matrix after enforcing zero-normal stress condition
g	normal gap function
ω_n	normal contact penalty parameter
ω_t	tangential slip penalty parameter

ACKNOWLEDGEMENTS

This research is partially supported by General Motors Corporation. This support is gratefully acknowledged.

REFERENCES

1. Gotoh M, Ishie F. A finite element analysis of rigid-plastic deformation of the flange in a deep-drawing process based on a fourth-degree yield function. *International Journal of Mechanical Sciences* 1978; **20**:423–435.
2. Wang NM, Budiansky B. Analysis of sheet metal stamping by a finite element method. *Journal of Applied Mechanics* 1978; **45**:73–82.
3. Wifi AS. An incremental complete solution of the stretch-forming and deep-drawing of a circular blank using a hemispherical punch. *International Journal of Mechanical Sciences* 1976; **18**:23–31.
4. Tang SC, Chu E, Samanta SK. Finite element prediction of the deformed shape of an automotive body panel during preformed stage. *NUMIFORM'82*. Pineridge: Swansea, 1982; 629–640.
5. Toh CH, Kobayashi S. Finite element process modeling of sheet metal forming of general shapes. *Grundlagen der Umformtechnik I*, Berlin, 1983; 39–56.
6. Toh CH, Kobayashi S. Deformation analysis and blank design in square cup drawing. *International Journal of Machine Tool Design and Research* 1985; **25**:15–32.
7. Belytschko T, Mullen R. Explicit integration of structural problems. *Finite Elements in Nonlinear Mechanics*, Tapir, Trondheim, Norway, 1977; 672–720.
8. Benson DJ, Hallquist JO. A simple rigid body algorithm for structural dynamics programs. *International Journal for Numerical Methods in Engineering* 1986; **22**:723–749.
9. Batoz JL, Guo YQ, Mercier F. The inverse approach including bending effects for the analysis and design of sheet metal forming parts. *NUMIFORM'95*. Balkema: Rotterdam, 1995; 661–667.
10. Makinouchi A, Nakamachi E, Onate E, Wagoner RH (eds). *Proceedings of the International Conference NUMISHEET'93*, Isehara, Japan, 1993.
11. Lee JK, Kinzel GL, Wagoner RH (eds). *Proceedings of the International Conference NUMISHEET'96*. The Ohio State University: U.S.A., 1996.
12. Gelin JC, Picart P (eds). *Proceedings of the International Conference NUMISHEET'99*, Besancon, France, 1999.
13. Yang DY, Oh SI, Huh H, Kim YH (eds). *Proceedings of the International Conference NUMISHEET'02*, Jeju, Korea, 2002.
14. Wenner ML. On work hardening and springback in plane strain draw forming. *Journal of Applied Metalworking* 1983; **2**:342–349.
15. Liu YC. The effect of restraining force on shape deviation in flanged channels. *Journal of Engineering Materials and Technology* 1988; **110**:389–394.
16. Karafillis AP, Boyce MC. Tooling and binder design for sheet metal forming processes compensating springback error. *International Journal of Machine Tools and Manufacturing* 1996; **36**:503–526.
17. Gan W, Wagoner RH. Die design method for sheet springback. *International Journal of Mechanical Sciences* 2004; **46**:1097–1113.
18. Gan W, Wagoner RH, Mao K, Price S, Rasouli F. Practical methods for the design of sheet formed components. *Journal of Engineering Materials and Technology* 2004; **126**:360–367.

19. Yang J, Jeon B, Oh S. Design sensitivity analysis and optimization of the hydroforming process. *Journal of Materials Processing Technology* 2001; **113**:666–672.
20. Naceur H, Guo YQ, Batoz JL, Knopf-Lenoir C. Optimization of drawbead restraining forces and drawbead design in sheet metal forming process. *International Journal of Mechanical Sciences* 2001; **43**:2407–2434.
21. Sosnowski W, Marczevska I, Marczewski A. Sensitivity based optimization of sheet metal forming tools. *Journal of Materials Processing Technology* 2002; **124**:319–328.
22. Choi KK, Yi K, Kim N-H, Botkin ME. Design sensitivity analysis of nonlinear shell structure with frictionless contact. *29th ASME Design Automation Conference, DETC2003/DAC-48795*, 2–6 September 2003, Chicago, IL.
23. Yi K, Choi KK, Kim NH, Botkin ME. Continuum-based design sensitivity analysis and optimization of nonlinear shell structures using meshfree method. *International Journal for Numerical Methods in Engineering* 2006; **68**:231–266.
24. Simo JC, Taylor RL. A return mapping algorithm for plane stress elastoplasticity. *International Journal for Numerical Methods in Engineering* 1986; **22**:649–670.
25. Hughes TJR, Winget J. Finite rotation effects in numerical integration of rate constitutive equations arising in large deformation analysis. *International Journal for Numerical Methods in Engineering* 1980; **15**:1862–1867.
26. Hughes TJR. Numerical implementation of constitutive models: rate-independent deviatoric plasticity. In *Theoretical Foundation for Large-Scale Computations of Nonlinear Material Behavior*, Nemat-Nasser S, Asaro RJ, Hegemier GA (eds). Martinus Nijhoff: Dordrecht, 1984.
27. Fish J, Shek K. Computational aspect of incrementally objective algorithms for large deformation plasticity. *International Journal for Numerical Methods in Engineering* 1999; **44**:839–851.
28. Saran MJ, Wagoner RH. A consistent implicit formulation for nonlinear finite element modeling with contact and friction. Part 1—Theory. *Journal of Applied Mechanics* 1991; **58**:499–506.
29. Saran MJ, Wagoner RH. A consistent implicit formulation for nonlinear finite element modeling with contact and friction. Part 2—Numerical verification and results. *Journal of Applied Mechanics* 1991; **58**:507–512.
30. Oden JT, Pires EB. *Nonlocal and Nonlinear Friction Laws and Variational Principles for Contact Problems in Elasticity*, vol. 50, 1983; 67–76.
31. Chang KH, Choi KK, Tsai CS, Chen CJ, Choi BS, Yu X. Design sensitivity analysis and optimization tool (DSO) for shape design applications. *Computing Systems in Engineering* 1995; **6**:151–175.
32. *MSC/PATRAN User's Guide*. The MacNeal-Schwendler Corp., 1999.
33. *DOT 5.0 User's Manual*. Vanderplaats Research & Development, Inc., 1999.